Structural evolution of high zirconia aluminosilicate glasses

M. Ficheux, E. Burov, G. Aquilanti, N. Trcera, V. Montouillout, L. Cormier

Structural evolution of high zirconia aluminosilicate glasses

M. Ficheux[a,b], E. Burov[a], G. Aquilanti[d], N. Trcera[c], V. Montouillout[e], L. Cormier[b,*]

[a]*Surface du Verre et Interface (UMR 125), CNRS/Saint-Gobain Research Paris, 39 quai Lucien Lefranc, 93300 Aubervilliers, France*

[b]*Sorbonne Université, CNRS UMR7590, MNHN, IRD, Institut de minéralogie, de physique des matériaux et de cosmochimie (IMPMC), 4 place Jussieu, F-75005 Paris, France*

[c]*Synchrotron SOLEIL, L'orme des merisiers, St Aubin BP48 F-91192, Gif-sur-Yvette cedex, France*

[d]*Elettra – Sincrotrone Trieste, 34149 Basovizza (TS), Italy*

[e]*CNRS CEMHTI-UPR3079, Univ. Orléans, Orléans F-45071, France*

Abstract

We report a detailed structural investigation of Ca-Na aluminosilicate glasses containing 0-20 wt% ZrO_2 using X-ray absorption spectroscopy, Raman spectroscopy and ^{27}Al and ^{29}Si NMR. The X-ray absorption spectroscopy data reveal that Zr is predominantly present in ZrO_6 octahedra but a significant Zr coordination change occurs with increasing ZrO_2 content. Though Al and Zr are competing to be surrounded by charge balancing cations, ^{27}Al NMR data do not show the presence of high-coordinated Al species; thus charge-balancing cations are preferentially localized close to AlO_4 tetrahedra rather than Zr polyhedra, explaining the increase in Zr coordination number that ultimately leads to limit Zr solubility in glasses. Raman and ^{29}Si NMR data indicates that Zr atoms are linked to the silicate network with a trend for higher degree of network connectivity at high zirconia content. Change in network connectivity and in Zr environment provide insights to understand chemical durability or crystallization in glasses.

*Corresponding author. Phone: +33 1 44 27 52 39

E-mail address: laurent.cormier@sorbonne-universite.fr (L. Cormier)

1.Introduction

Zirconium is encountered as a key constituent element of High Level Waste (HLW) glasses, coming both as a fission product and from fuel cladding materials of zirconium alloys [1], and it can be present in high concentration near the refractory-melt interface in industrial furnaces [2]. Zr has beneficial effects on glass properties, improving chemical durability or mechanical resistance, increasing viscosity and decreasing thermal expansion [3][4][5][6][7].

Zr can adopt variable environment in glasses depending on its content or network polymerization as investigated by numerous X-ray absorption studies [1][8][9][10][11][12][13]. Zr is typically observed in ZrO_6 octahedra ($^{[6]}Zr$) in alkali silicate and aluminoborosilicate glasses. High coordinated Zr species such as seven-fold ($^{[7]}Zr$) and eight-fold ($^{[8]}Zr$) coordinated sites have been also observed and their presence can be explained by a deficit of charge balancing cations which are required to ensure charge compensation of $(ZrO_6)^{2-}$ sites [13]. The presence of $^{[8]}Zr$ has been reported within highly polymerized glasses [8] while $^{[7]}Zr$ has been suggested at high ZrO_2 content in alkali borosilicate glasses [14]. $^{[7]}Zr$ has been observed as the dominant species in Mg aluminosilicate glasses [15] and this coordination number was also suggested in a Ca aluminosilicate glass [11]. These high coordinated species could trigger the nucleation of ZrO_2, which is encountered in the formation of glass-ceramics [16]. Indeed, Zr is an efficient nucleating agent, whose environment is essential to understand the first stages of nucleation in glasses [17][18].

Very few studies have investigated glasses with high ZrO_2 content, though understanding the Zr local environment is important to increase zirconia solubility while controlling the crystallization occurring near saturation. Only borosilicate glasses with high ZrO_2 levels, up to 25 wt%, have been investigated [14][4][19] as well as high-zirconia glass fibers (soda silicate glass containing about 16 wt% ZrO_2), used for cement reinforcement due to high alkali durability [20]. However, higher ZrO_2 concentration can be obtained for amorphous materials prepared via a sol-gel route [21][22][23]. Saturation of ZrO_2 in glasses depends strongly on

compositions with a trend towards a higher solubility in depolymerized glasses, containing typically high amounts of alkali oxides [24][8].

In this contribution, we have considered glasses in the Na_2O-CaO-Al_2O_3-SiO_2 system up to domains at the limits of saturation in ZrO_2. This limit has been firstly investigated using predictive thermodynamic calculations with a quasi-chemical model and, in a second time, by the characterization of glasses using complementary structural methods, X-ray absorption spectroscopy (XAS), Raman spectroscopy and high-field ^{27}Al and ^{29}Si NMR. We report the modification around Zr environment and the evolution of the aluminosilicate network.

2. EXPERIMENTAL

2.1. Sample composition and preparation

Reagent grade raw materials (<0.01wt% impurities) were weighted according to glass compositions reported in Table 1, in order to prepare a batch of 10 g. The 0Zr composition is chosen close to that of a window glass. To decrease the composition uncertainty, the humidity of raw materials has been controlled and $CaCO_3$ and Na_2CO_3 powders have been decarbonized at 780 °C during 10 hours. The mixtures was melted in Pt crucibles at 1550 °C during 4-6 h in air using an electric furnace. The liquid was quenched by immersing the bottom of the crucible into water and then mechanically fractured and crushed. The powder was remelted in the same conditions to enhance glass homogeneity.

The chemical compositions were determined by Electron Probe Micro-Analysis (EPMA) using a Cameca SX-Five electron microprobe at the CAMPARIS center (Sorbonne University, Paris). An accelerating voltage of 15 kV and a beam current of 10 nA were used. The values in Table 1 are the average of 10 different measured points. A short counting time 5 s was chosen to limit alkali migration during acquisition. The sample name referred to the wt% of ZrO_2 in the glass, 5ZrAl corresponds thus to the glass containing 5wt% ZrO_2.

Table 1. Glass composition determined by quantitative EPMA analysis (the standard deviation is in parenthesis).

	SiO_2 Mol%	Al_2O_3 Mol%	Na_2O Mol%	CaO Mol%	ZrO_2 Mol%
0ZrAl	67.45 (0.83)	6.96 (0.22)	13.48 (1.34)	12.11 (0.21)	-
5ZrAl	67.65 (0.82)	7.20 (0.22)	10.46 (1.31)	11.86 (0.12)	2.83 (0.33)
7.5ZrAl	65.30 (0.50)	6.87 (0.24)	12.33 (0.22)	11.36 (0.15)	4.14 (0.13)
10ZrAl	65.5 (1.06)	7.04 (0.71)	11.95 (0.63)	10.45 (0.35)	5.06 (0.24)
12ZrAl	63.32 (0.25)	6.64 (0.15)	12.14 (0.09)	11.35 (0.07)	6.55 (0.23)
15ZrAl	62.72 (0.28)	6.37 (0.09)	11.62 (0.11)	11.31 (0.16)	7.98 (0.29)
16ZrAl	64.67 (1.06)	6.30 (0.71)	9.28 (0.63)	11.10 (0.35)	8.65 (0.24)

2.2. Structural methods

To be able to characterize the glass structure at different scales and to obtain the complete picture of Zr integration in the alumino-silicate glass structure, we combine several structural methods.

2.2.1. X-ray absorption spectroscopy

XANES (X-ray absorption near edge structure) data were collected at the Zr $L_{2,3}$-edges on the LUCIA beamline [25] at the SOLEIL synchrotron facility (Saint-Aubin, France) using a Si(111) double crystal monochromator with a current in the storage ring of 500 mA and an energy of 2.75 GeV. Data were recorded in fluorescence yield (FY) mode using a silicon drift detector and total electron yield (TEY) mode using the sample drain current in vacuum at ambient temperature. Each spectrum is the average of at least two acquisitions with an energy step of 0.2 eV near the edge at a counting time of 3 seconds. XANES spectra were obtained for crystal references containing Zr in different environments: Baghdadite ($Ca_3ZrSi_2O_9$) contains a distorted ZrO_6 site with six different Zr-O distances spanning from 1.97 Å to 2.20 Å [26], Baddeleyite (monoclinic ZrO_2) contains a distorted ZrO_7 site with Zr-O distances ranging between 2.05-2.28 Å [27], and zircon ($ZrSiO_4$) contains a ZrO_8 site with two Zr-O distances at

2.13 Å and 2.27 Å [28]. FY spectra are reported in this paper except for m-ZrO_2 and zircon for which TEY-XANES spectra are presented.

After normalization of the high energy side using Athena software [29], a residual background simulating the edge-jump was subtracted by fitting an arctangent function. The background-free spectra have then been fitted with two pseudo-voigt functions. The parameters of the pseudo-voigt functions give information on the 4d energy levels that are sensitive to the coordination number.

XANES and EXAFS (Extended X-ray absorption fine structure) spectra were recorded at Zr K-edge on the XAFS beamline [30] of the Elettra synchrotron facility (Italy), with electron storage ring operating at 2 GeV and 310 mA. Synchrotron radiation was monochromatized with a Si(111) double crystal monochromator to scan over the Zr K-edge for the spectral range of 17.7-19.5 keV. The data were collected in transmission mode using ionization chambers filled with a mixture of different gases in order to have 10%, 70% and 95% of absorption in the I_0, I_1 and I_2 chambers respectively. A Zr foil was used for energy calibration in each scan. A typical scan lasts ~30 min and 3 scans were measured and averaged to give the signal in transmission mode using a N_2 flow cryostat at a fixed T~77 K. Background corrections and normalization was obtained using Athena software [29]. The extraction of the EXAFS signals, $\chi(k)$, was also processed using Athena program by removal of a spline-smoothing function, and r-space EXAFS spectra were obtained by calculating the Fourier Transform (FT) of the $k^3\chi(k)$ signals in the (2.5-14) $Å^{-1}$ k-range using a Hanning function.

The·$\chi(k)$ EXAFS data were analyzed using ARTEMIS software [29]. The electronic parameters (passive electron reduction factor S_0^2, electron mean free path $\lambda(k)$, backscattering phase $\Phi(k,2\pi)$ and amplitude $f(k,2\pi)$) were obtained by *ab initio* multiple scattering calculations using FEFF7 software [31] and considering structural crystalline models. EXAFS spectra were fitted by adjusting the three structural parameters, interatomic distance R, coordination number N, and the corresponding Debye–Waller factor σ^2. The S_0^2 and ΔE_0 (energy shift of the photoelectron) were also determined.

2.2.2. Raman spectroscopy

Raman spectroscopy was used to determine the average changes in network connectivity induced by ZrO_2 addition. Raman spectra were acquired using a Renishaw Qontor spectrometer with a green laser of 532 nm wavelength and 50 mW power for 10 seconds with 10 repetitions.

The spot was focused with a Leica x50 lens, giving an excited zone of about 5µm². The temperature and frequency dependence were corrected using the Long correction [32]. The spectra were normalized using the total area under the spectrum in the range 200-1400 cm^{-1}.

2.2.3. Nuclear magnetic resonance (NMR) spectroscopy

The ^{27}Al high-resolution NMR experiments have been conducted at 20.0 T (850 MHz) on a Bruker AVANCE spectrometer equipped with high-speed MAS probe head (spinning rates 30 kHz, aluminum free zirconia rotors of 2.5 mm diameter). 1D MAS spectra have been acquired after a single short pulse ($\pi/10$) ensuring a quantitative excitation and quantification of ^{27}Al central transition. Chemical shifts were referenced relative to $Al(NO_3)_3$ 1M solution. ^{29}Si NMR experiments were conducted at 9.4 T (400 MHz) on a Bruker AVANCE I spectrometer using a 4 mm double resonance MAS probehead. The ^{29}Si quantitative MAS spectra were recorded at a spinning frequency of 10 kHz with a pulse duration of 2.4 μs (corresponding to a flip angle of 30°) and a recycle delay of 60 s. Chemical shifts were referenced relative to TMS. The spectra have been simulated using DMfit software [33].

3. Thermodynamics predictions and Zr solubility

Thermodynamic calculations were performed using FactSage® software and a quasichemical model optimized for oxide glasses in order to determine the stability phase domains with increasing ZrO_2 content. We have chosen a non-exhaustive list of nine crystalline phases that are expected to crystallize in our system: nepheline ($NaAlSiO_4$), anorthite ($CaAl_2Si_2O_8$), wollastonite ($CaSiO_3$), mullite ($2Al_2O_3$-SiO_2), cristobalite (SiO_2) as well as several crystalline phases containing zirconium, zircon ($ZrSiO_4$), the tetragonal low temperature form of ZrO_2, monoclinic zirconia (m-ZrO_2) and cubic zirconia (c-ZrO_2).

In the temperature range 600-1600 °C, the activity of glasses and of the nine crystalline phases is calculated (Fig. 1), indicating the domains of stability for each phases. The composition is expressed in wt% ZrO_2 in the formulation. The variation of the ZrO_2 content is at the expense of the other four oxides whose relative ratios are constant, which means that, when 1 wt% ZrO_2 is added, the sum of all other oxides is reduced by 1 wt% in the composition, maintaining the mass ratios between the different oxides.

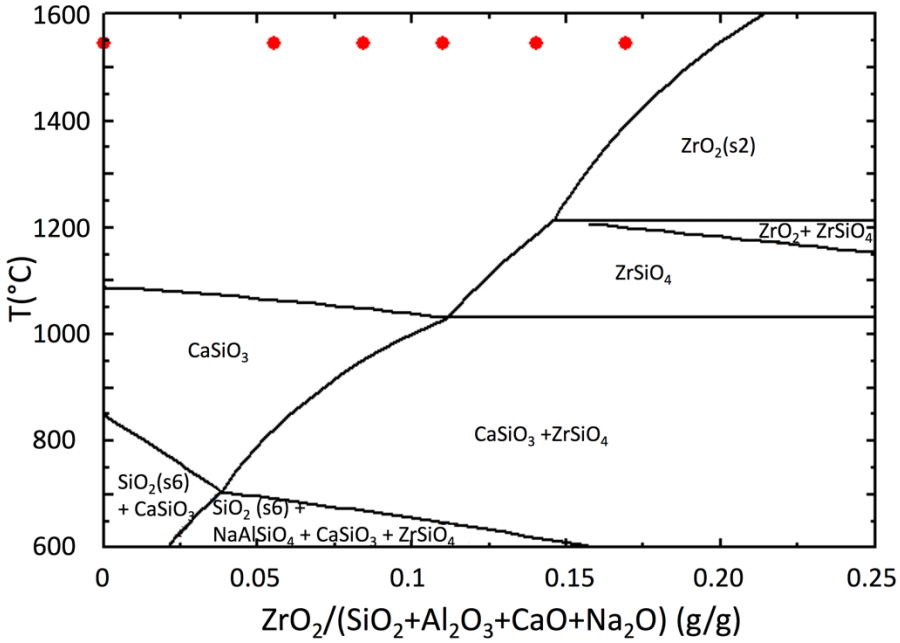

Fig. 1. Phase diagram in a Na_2O-CaO-Al_2O_3-SiO_2-ZrO_2 system with increasing ZrO_2 content (wt%). ZrO_2(s2)=t-ZrO_2, ZrO_2=m-ZrO_2, SiO_2(S6)=cristobalite. The red points correspond to the ZrO_2 content

The solubility limit of ZrO_2 between 1400-1600 °C is expected to be 13-16 wt%. We selected the glass composition in this domain to get completely homogenous samples (red points in Fig.1). We successfully obtained glasses containing up to 15 wt% ZrO_2 before observing saturation and crystallization. The melting temperature was set at 1550 °C and an increase of the melting temperature could allow the incorporation of more ZrO_2, as suggested by Fig. 1. This saturation value is close to the 17-18 wt% predicted by the literature for similar compositions [24] and is consistent with the thermodynamic predictions. In borosilicate glasses, zirconia content is higher and can reach up to 21 wt% before crystallization [14][4].

Another point of consideration is that at lower ZrO_2 content, crystallization of wollastonite and nepheline is expected during cooling down of these compositions. To avoid it, our glasses were quenched by removing the liquid from the furnace and immersing the bottom of the crucible into water. This was sufficient to bypass the crystallization, indicating that nucleation and crystal growth have slow kinetics.

The ZrO_2-free composition 0ZrAl (Table 1) represented in Fig. 1 was used to compare thermodynamic predictions with a real sample. DSC measurements (Fig. 2) show a single large crystallization peak at 1043 °C and the melting of crystals at 1204 °C. The glass transition

temperature is determined at 711°C. X-ray diffraction and Raman spectroscopy indicate the crystallization of wollastonite in this sample, as predicted by the thermodynamics calculations Fig. 1). Consistent with these predictions, no crystals containing zirconium, such as zirconia or zircon, have been found. However, the appearance of zirconium-carrying crystals in this composition domain is well known from glass manufacturers who can occasionally find them in the form of millimeter defects on the finished products [34,35]. Interactions in industrial compositions are much more complex than in our simple model due to more complex compositions and the much longer and variable thermal cycles in the glass melting furnace.

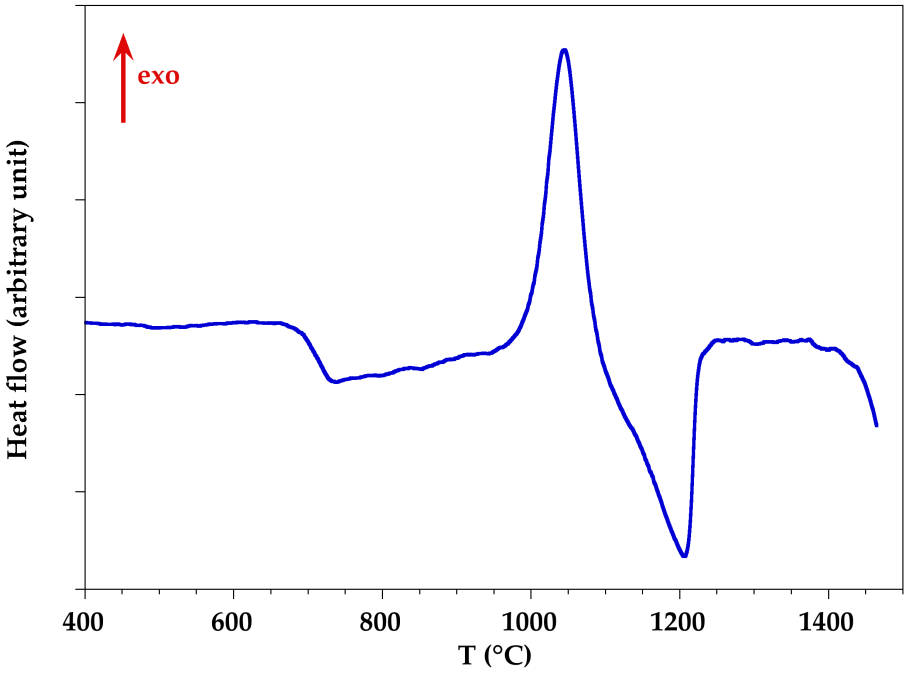

Fig. 2. DSC curve of the 0ZrAl glass composition.

Regarding the glass saturation with zirconium, glasses containing up to 15 wt% ZrO_2 can be synthesized without observing crystallization. Crystallization was detected on the 16ZrAl sample by scanning electron microscopy (SEM) observations (Fig. 3), revealing two phases whose compositions were acquired by Electron Probe Micro-Analysis (EPMA). Note that the black area corresponds to the resin in which the crushed glass was inserted. The grey regions in Fig. 3 correspond to the glass, saturated in ZrO_2 with 15.7 wt% in average according to EPMA analysis, which is consistent with thermodynamics calculations. The white regions correspond to ZrO_2 crystals. Zirconium in excess crystallizes in ZrO_2 above the saturation limit in agreement with thermodynamics calculation at 1500°C. The fast temperature decrease during

quenching probably prevents the formation of zircon, which is predicted in the phase diagram in Fig 1.

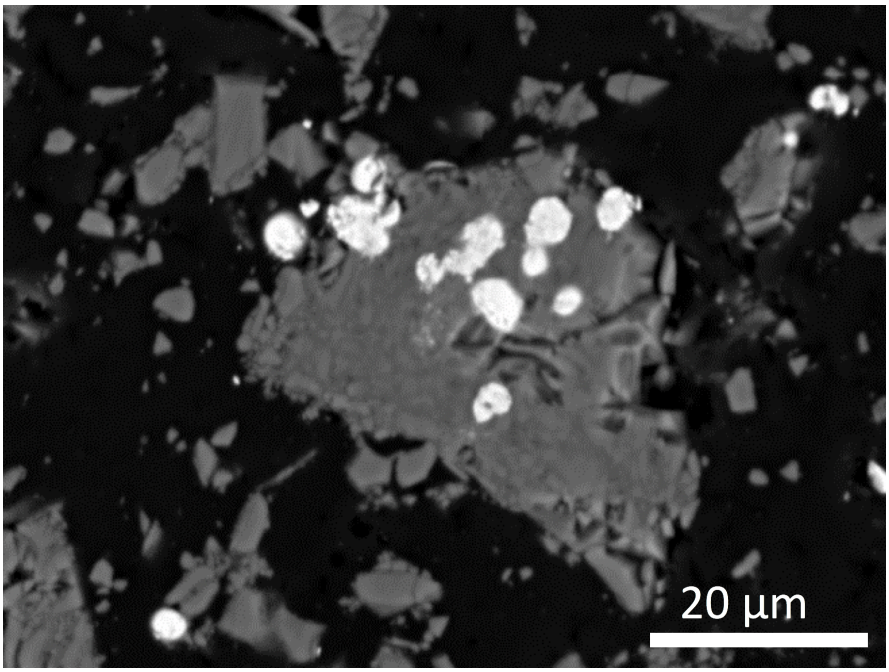

Fig. 3. SEM image of the 16ZrAl glass sample. Saturated glass at 15/16 wt% ZrO_2 in grey and ZrO_2 crystals formed by excess Zr in white.

4. Experimental results

4.1. Zr environment from XAS spectroscopy

4.1.1. XANES at Zr $L_{2,3}$-edges

XANES spectra at $L_{2,3}$-edges are shown in Fig. 4 for the three crystalline references: baghdadite ($Ca_3ZrSi_2O_9$), baddeleyite (m-ZrO_2) and zircon ($ZrSiO_4$). The Zr $L_{2,3}$ edges are due to transition from 2p to 4d states. In Oh symmetry, each edge is composed of two peaks associated with the crystal field splitting of the 4d states into t_{2g} and e_g empty states. The energy levels of these states lead to the two energy positions that can be well separated contributions or overlapped contributions. The previous studies on these materials [13][36][37] showed that

energy positions and relative intensities of the t_{2g} and e_g levels depend strongly on the site symmetry and thus on the coordination number and, in a second order, on the site distortion.

The two t_{2g} and e_g energy levels are well separated on the spectra of baghdadite in which zirconium is in six-fold coordination. The energy position of the two peaks gives an apparent crystal field splitting of 2.8 ± 0.2 eV. The two energy levels are less resolved for Baddeleyite containing Zr in 7-fold coordination due to the important site distortion and the poor symmetry of this site [38]. A lower crystal field splitting of 2.2 ± 0.2 eV is observed. Finally, in zircon containing zirconium in 8-fold coordination, the two bands are almost merged. The L_2-edge spectra show the same behavior although the data have a lower quality. These results are consistent with previous observations and multiplet calculations [10].

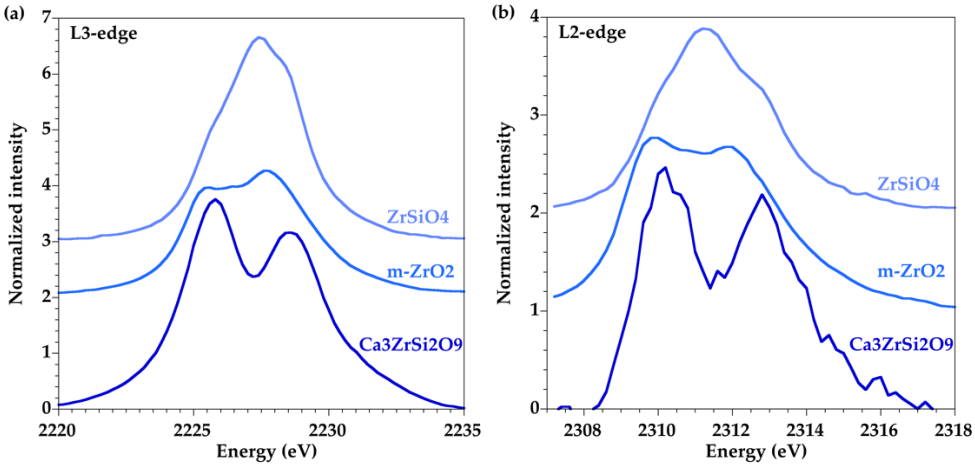

Fig. 4. XANES spectra of crystalline references at the Zr L_3 (a) and L_2 (b) edges.

XANES spectra at $L_{2,3}$-edges are shown in Fig. 5 for the studied glasses. L_3-edge spectra present also a better signal/noise ratio than L_2-edge spectra. Each of these spectra shows two well-resolved features. However, the spectra evolve with the addition of ZrO_2. To better quantify these changes, the t_{2g} and e_g levels were fitted using pseudo-Voigt functions. The position, area and FWHM (full width at half maximum) for the two peaks of each edge are shown in Fig. 6. The apparent crystal field splitting for glasses is very close to those of Ca_3ZrSiO_9 (this study) and elpidite ($Na_2ZrSi_6O_{15}.3H_2O$ [13]) that both present $^{[6]}Zr$ sites. Evolution of the peak position (Fig. 6b) indicates that the energy levels do not vary significantly with the ZrO_2 content. Therefore the apparent crystal field splitting is not strongly modified. These results indicate predominant $^{[6]}Zr$ sites. However, the measured area of each peak

decreases while the FWHM increases with the addition of ZrO_2 and this effect is more important for the ZrO_2-richest glass (15ZrAl and 16ZrAl). This broadening fills the gap between the two peaks, which can be associated with the distortion of the zirconium sites or a change in coordination number.

A deconvolution of the XANES spectra can be performed using a linear combination of the XANES spectra representative for $^{[6]}Zr$ and $^{[7]}Zr$ [36]. The spectrum of 5ZrAl glass has been considered as representative of $^{[6]}Zr$. Indeed, the Baghdadite spectrum cannot fit the spectrum of 5ZrAl and it cannot be used as a reference for $^{[6]}Zr$ since the FWHM of the two peaks are too large due to the strong deformation of the ZrO_6 site in this crystalline compound. This indicates that a high symmetry ZrO_6 site exists in the 5ZrAl, as observed in previous EXAFS analysis in borosilicate glasses [9]. For the other glasses (except 16ZrAl), a linear combination indicates between 10-20% of high coordinated Zr species (Table 1 in Supplementary Information). Different combinations of m-ZrO_2 and $ZrSiO_4$ spectra, as representative models for highly coordinated Zr, and of 5ZrAl spectrum, as representative model for the $^{[6]}Zr$, lead to statistically equivalent fits. This indicates that it is not possible to discriminate between $^{[7]}Zr$ and $^{[8]}Zr$. For the 16ZrAl spectra, the amount of $^{[6]}Zr$ is the smallest with only 56%. This is consistent with the steep decrease in intensity and broadening of the L_3 peaks. This also agrees with the Zr solubility limit for this composition.

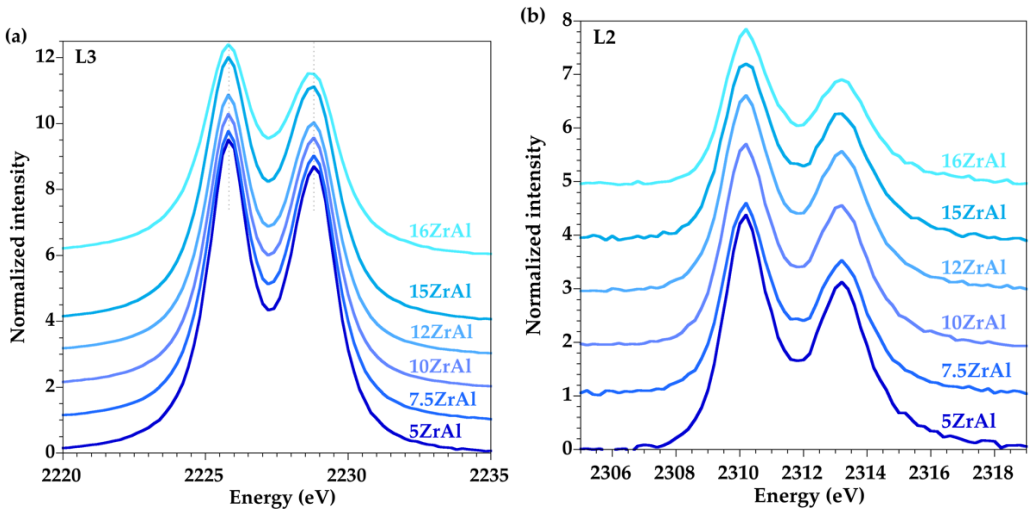

Fig. 5. XANES spectra at the Zr L_3 (left) and L_2 (right) edges for glasses with different ZrO_2 contents.

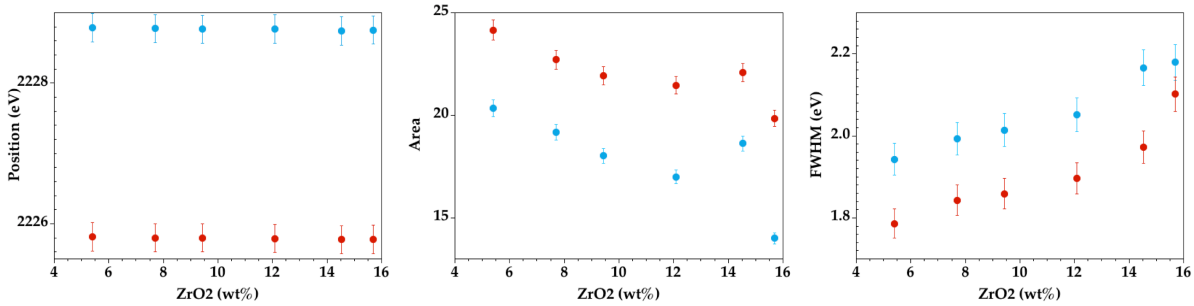

Fig. 6. Peak parameters obtained by fitting the L_3 edges using pseudo-Voigt functions as a function of ZrO_2 content. The values corresponding to the energy level of the first band (low energy) are in red when those corresponding to the energy level of the second band (high energy) are in blue.

4.1.2. XANES and EXAFS at Zr K-edge

XANES spectra at Zr K-edge of crystalline compounds and glasses are plotted in Figure 7. The feature A is attributed to a transition from 1s energy levels to Zr_{4d}/O_{2p} molecular orbitals [39][40]. It occurs for site geometries without a center of symmetry and its intensity is thus enhanced for distorted sites. In references, the feature A is apparent for m-ZrO_2 and is associated with site distortion. Since it is rather weak for the spectra of the glasses, this indicates a small site distortion of the Zr sites. The main resonance after the onset of absorption is split into two contributions B and C. Their attribution is not straightforward as they result from multiple scattering processes that cannot be simply related to a structural feature. Their evolution compared to the references is usually used considered [16,37]. The C component is more intense than the B one for $^{[6]}$Zr crystalline model compounds [1][10] as well as in the spectrum of Baghdadite measured in this work. These two features are not well separated for Baddeleyite but the general trend is that the peak B is more intense than the peak C for $^{[7]}$Zr and $^{[8]}$Zr references. All the XANES spectra of the glasses are similar to each other and close to that observed for Baghdadite. The relative intensities of peaks B and C are consistent with $^{[6]}$Zr as the dominant coordination species in the glasses investigated, but the peak C is less intense in glasses compared to the $^{[6]}$Zr reference, which indicates possible site distortion or high coordinated sites. Given the small intensity of peak A, the latter explanation is preferred. Finally the feature D is the first EXAFS oscillations that appear in Figure 8a.

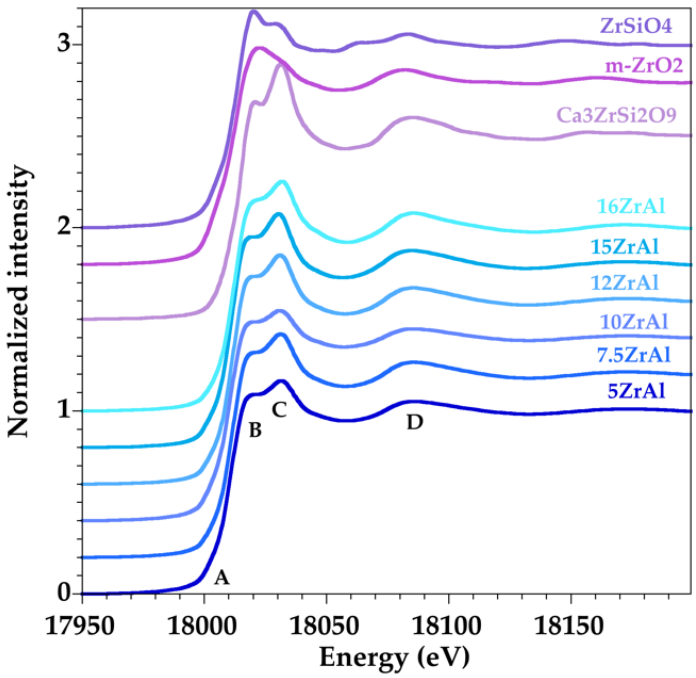

Fig. 7. XANES spectra at Zr K-edge for crystalline references and glasses.

The extracted Zr K-edge EXAFS oscillations are shown in Fig. 8 with the modulus of the Fourier transform of the $k^3\chi(k)$ signals for the Zr-containing glasses. The EXAFS spectra acquired on each glasses are similar and do not show significant differences. The EXAFS oscillations can be fitted using different parameters for each scattering path: interatomic distance, R, coordination number, N, and Debye-Waller factors including both structural and thermal disorder, σ^2. The structural information for the Baddeleyite crystal was used to fit the EXAFS spectrum up to 4 Å using single scattering paths of each neighboring shells around the absorbing element (Fig. 9). The scattering paths are generated using Feff code [31]. The fit gives R and N values in agreement with crystallographic data determined by X-ray diffraction and allows the determination of the reduction factor, $S_0^2 = 0.648 \pm 0.002$, which is the value used for the glass spectra analysis.

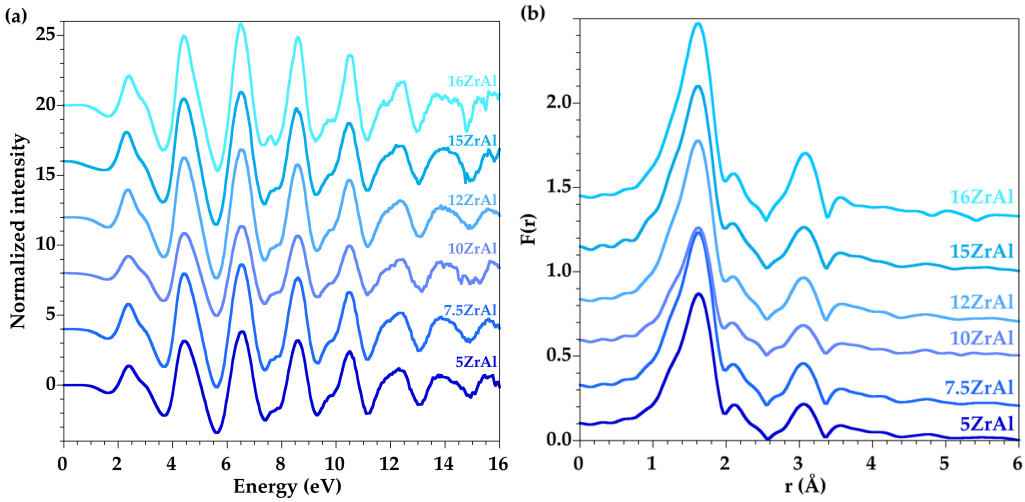

Fig. 8. (a) Zr K-edge k^3-weighted EXAFS spectra and (b) modulus of the Fourier transform of the k^2-weighted EXAFS signals.

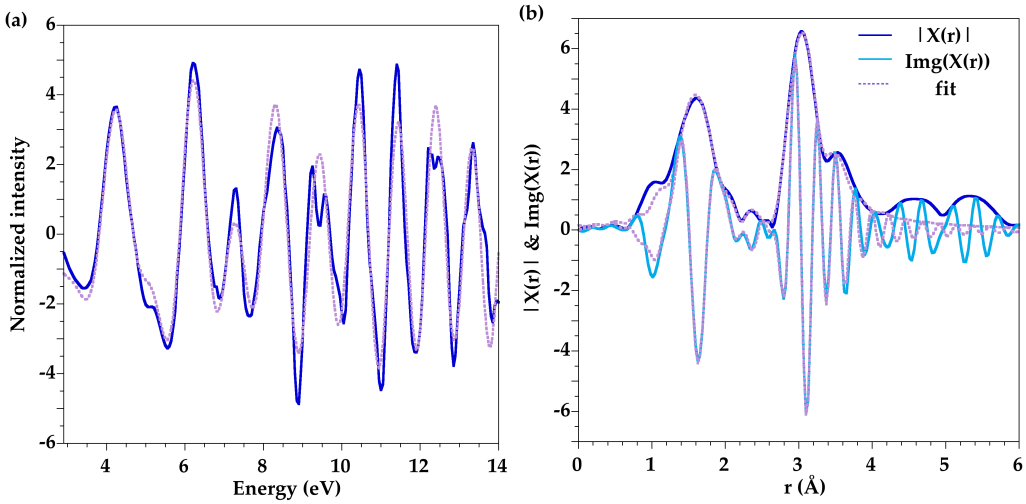

Fig. 9. Real and imaginary part of the EXAFS spectrum of the Baddeleyite reference used for the determination of S_0^2. The blue and purple curves correspond to the measurement and the fit, respectively.

For the fit of EXAFS spectra for each glass, it is necessary to determine the best combination of diffusion paths and, for each path, R, N and σ^2 values. The following single scattering paths were selected: the first neighbor oxygen diffusion path of the Baddeleyite [41]; second (Al/Si) neighbors at 2.99 Å of zircon; second Zr neighbors at 3.4 Å of Baddeleyite. It is not possible to make the difference between Al or Si neighbors due to their close atomic numbers. For each shell, the coordination number (N), interatomic distances (R), and Debye-Waller (σ) factors

were refined and the fitted values are grouped in Table 2, as well as the error factor R-factor. The accuracy on the determination of the coordination number is on the order of ±0.3, so the slight variations that we observe are exploitable with caution. The accuracy of the interatomic distances and Debye Waller factors (shown in parenthesis in Table 2) are based on the layer under consideration.

Table 2. Structural parameters used to fit the glass EXAFS spectra for three shells of neighbours (O, Al/Si and Zr) with R the interatomic distance, σ the Debye-waller factor, N the coordination number and R-factor the goodness of fit parameter. The error is in parenthesis on the last digit. The error on the coordination number is ±0.3.

	O			Al/Si			Zr			
	N	R (Å)	σ^2 (Å^2)	N	R (Å)	σ^2 (Å^2)	N	R (Å)	σ^2 (Å^2)	R-factor
5ZrAl	5.9	2.08(1)	0.005(5)	3.3	2.91(1)	0.006(3)	1.4	3.32(4)	0.030(5)	0.011
7.5ZrAl	6.1	2.08(1)	0.004(5)	3	2.91(1)	0.005(5)	1.5	3.37(4)	0.021(5)	0.016
10ZrAl	5.9	2.08(1)	0.006(5)	2.8	2.90(1)	0.006(5)	1.1	3.34(3)	0.029(4)	0.013
12ZrAl	6.3	2.08(1)	0.004(5)	3	2.91(1)	0.005(4)	1.2	3.38(3)	0.026(5)	0.023
15ZrAl	6.4	2.09(1)	0.004(5)	3	2.93(1)	0.005(5)	1.5	3.40(3)	0.032(6)	0.034

The coordination number of the oxygen atoms around zirconium increases from 6 to 6.4 as the ZrO_2 content increases. In view of our accuracy, this change is small but can correspond to the predictions of the thermodynamic analysis (Fig. 1), i.e. the formation of a very small amount of ZrO_2, even below the saturation threshold. This is consistent with the apparition of $^{[7]}$Zr sites, which were also suggested in the analysis of the $L_{2,3}$-edges XANES spectra, though $^{[6]}$Zr is the predominant species in all glasses investigated. The Zr-O mean interatomic distance is 2.08 ± 0.01 Å in agreement with previous investigations [1][10][14][39]. The second shell of Al/Si neighbors has a relatively stable coordination number of 3 with a Zr-Si/Al distance around 2.91 ± 0.01 Å which increases slightly to 2.93 Å at high ZrO_2 content. This distance is small compared to the Zr-Si distances obtained in borosilicate glasses, 3.4 ± 0.1 Å [10][42], for which

corner-sharing polyhedra between SiO_4 and ZrO_6 units are considered. The short distance observed for aluminosilicate glasses implies edge-sharing polyhedral linkages that exist in zircon but involve a cubic Zr site. A similar model has already been proposed for aluminosilicate glasses [37]. Finally, a contribution from a third shell corresponding to Zr neighbors was required to get a good fit. This contribution indicates that Zr-O-Zr connections exist, even with only 5wt% ZrO. For this Zr second neighbor shell, the interatomic distance increases significantly with ZrO_2 content from 3.32 Å for 5 wt% ZrO_2 to 3.40 Å for 15 wt% ZrO_2. The number of zirconium neighbors is small ~1.4 and this value does not vary significantly with the ZrO_2 content.

4.2. Raman spectroscopy

Raman spectra for the five glasses are shown in Fig. 10. The 400-600 cm^{-1} region corresponds to the bending vibrations of the Si-O-Si bonds. The 500 cm^{-1} band shifts towards higher wavenumbers with increasing Zr content. This can be associated with Zr atoms deforming the silicate network and modifying the ring statistics [5] or to the crystallization of ZrO_2-contaning phases [43].

Major changes are observed in the 850-1200 cm^{-1} region that corresponds to the stretching modes of the Si-O bond within the SiO_4 tetrahedra forming Q^n units (*n* is the number of bridging oxygen). This region gives a good qualitative, and sometimes quantitative, estimate of the degree of connectivity in glasses. Between the different Raman spectra, the intensities of the bands at 980 cm^{-1} and 1080 cm^{-1} are those evolving the most. Indeed the band at 1080 cm^{-1} decreases in intensity as the concentration of zirconium increases and, concomitantly, the intensity of the band at 980 cm^{-1} increases. The 1080 cm^{-1} band is commonly attributed to the characteristic vibration of the Q^3 species. The 980 cm^{-1} band is less common and has already been assigned to the Si-O-Zr vibration in a borosilicate glass [42][43][44]. Following Quintas et al., this band is ascribed to Q^3 SiO_4 units associated with one ZrO_6 octahedron (a silicon atom linked to three second neighbors silicon and one zirconium neighbor) and is noted $Q^3(Zr)$.

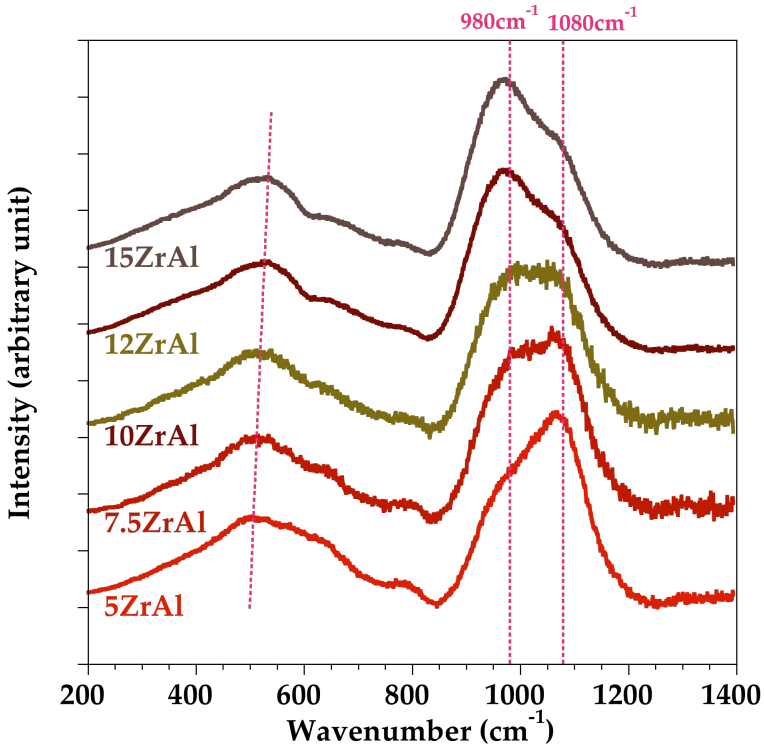

Fig. 10. Raman spectra acquired on glasses. Some spectra have been displaced for clarity. Lines indicate the shift of the band at ~500 cm^{-1} and the position of the bands at 980 cm^{-1} and 1080 cm^{-1}.

4.3. ^{27}Al and ^{29}Si NMR spectroscopy

^{27}Al high-field and ^{29}Si NMR measurements were conducted to investigate the influence of zirconium content on aluminum and silicon environments (Fig. 11).

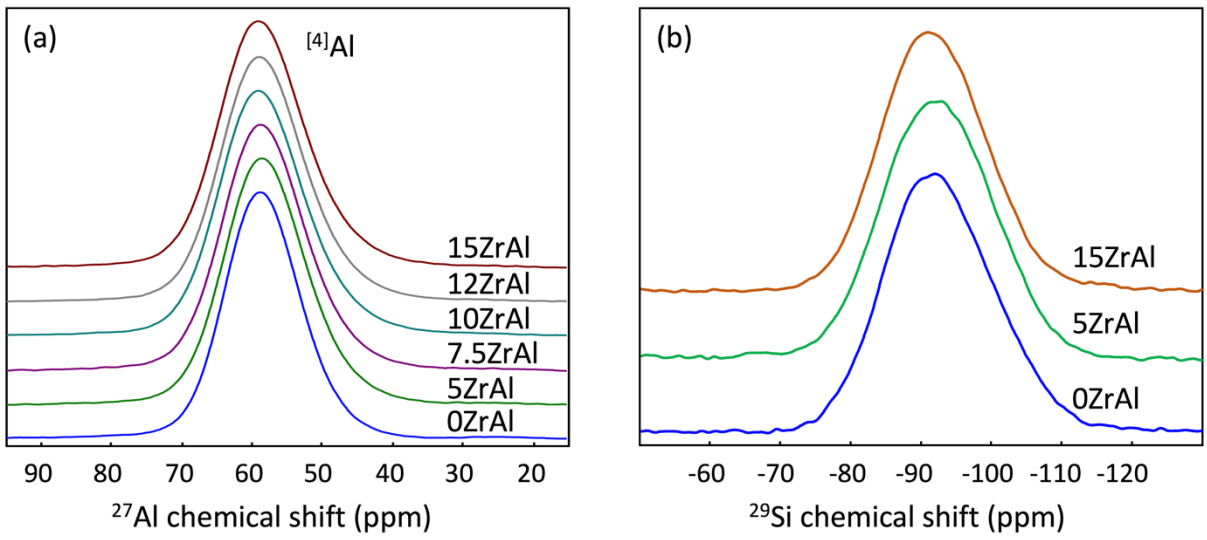

Fig. 11. (a) ^{27}Al and (b) ^{29}Si MAS-NMR spectra of the different glasses.

Table 3: NMR parameters estimated from simulation of ^{27}Al NMR spectra: isotropic chemical shift (δ_{iso}) quadrupolar coupling constant (C_Q) and distribution of chemical shift (ΔCS).

Sample	δiso (ppm) ± 0.1 ppm	C_Q (kHz) ± 1 kHz	ΔCS (ppm) ± 0.1 ppm
0ZrAl	62.0	4634	10.3
5ZrAl	62.4	5101	11.0
7.5ZrAl	62.6	5114	11.2
10ZrAl	63.1	5339	11.1
12ZrAl	62.8	5280	11.0
15ZrAl	63.1	5326	11.3

^{27}Al NMR spectra show a single signal centered near 60 ppm consistent with aluminum in tetrahedral configuration. The asymmetric lineshape is typical of disordered materials exhibiting a distribution of both the quadrupolar interaction, C_Q, and the isotropic chemical shift, δ_{iso}. No five- or six-fold coordinated Al species could be detected. The spectra have been simulated using Gaussian distribution of δ_{iso} and a Gaussian isotropic model for the distribution of the quadrupolar interaction parameters C_Q and η_Q (Czeckj model implemented in the DMfit software [33]). The values of NMR parameters are grouped in Table 3. In the case of 0ZrAl, the NMR parameters, especially the C_Q value of 4.6MHz, is coherent with a tetrahedral aluminum charge compensated by Na^+ [45]. As the ZrO_2 content increases, we observe an increase of both isotropic chemical shifts and quadrupolar coupling constants up to 5.3MHz for ZrAl15. This indicates that an increasing part of aluminum is compensated by cation with a higher field strength than Na^+, in this case probably Ca^{2+} [46].

^{29}Si NMR spectra (Figure 11) show a broad resonance centered at around -92 ppm associated with the overlapping of different Q^n species. In aluminosilicate glasses, various chemical

environments around Si (Q_m^n with m the number of Al second neighbors) do not allow a clear separation of the different contributions. The presence of Zr adds another complexity due to the possibility of Si-O-Zr bonds as detected by Raman spectroscopy. Table 4 summarized the chemical shifts and the FWHM determined by fitting the spectra for three glasses. A slight shift of the peak towards positive chemical shifts is observed, associated with a narrowing when the ZrO_2 content increases. We can note a similar trend in aluminoborosilicate glasses [44]. The effect is small and does not allow us to quantify a difference in distribution between the Q^n species. However a chemical shift around -90 ppm is coherent with a majority of Q^3 species charge compensated by Ca^{2+} and the shift towards positive values suggests a slight decrease in polymerization.

Table 4: NMR parameters estimated from simulation of ^{29}Si NMR spectra: chemical shift of center of gravity (δ_{CG}) and full weight hlf maximum (FWHM).

Sample	δ_{CG} (ppm) ± 0.1 ppm	FWHM (ppm) ± 0.1 ppm
ZrAl0	-92.2	18.2
ZrAl5	-92.2	18.5
ZrAl15	-91.5	17.2

5. Discussion

5.1. Zr local environment

XANES spectra at Zr K- and $L_{2,3}$-edges and EXAFS signals at Zr K-edge give consistent information on the Zr environment. The majority of Zr atoms are localized in ZrO_6 octahedra with probably a small distortion compared to Zr environment in Baddeleyite and given the small σ^2 values for the first Zr-O shell (Table 2). As the ZrO_2 content increases, a significant evolution is put in evidence with an increasing proportion of $^{[7]}$Zr and possibly $^{[8]}$Zr sites. As XRD patterns

do not exhibit Bragg peaks (except for 16ZrAl glass), these high coordinated Zr species remain in amorphous environments. For the 15ZrAl the proportion of $^{[7]}$Zr and $^{[8]}$Zr is ~20% (see Table Si1), at the limit of Zr solubility. For 16ZrAl, an approximate equal amount of $^{[7]}$Zr and $^{[8]}$Zr up to 45% is detected but this glass contains ZrO_2 crystals.

The presence of ZrO_8 units has been reported in polymerized glasses such as albite glass ($NaAlSi_3O_8$) and was an indication of saturation of the melt in Zr [39]. ZrO_7 units were also observed in Ca and Mg aluminosilicate glasses [37][15][12][11]. In the SiO_2-Al_2O_3-MgO-ZnO-ZrO_2 system, EXAFS analysis indicate edge-sharing linkages with SiO_4 or AlO_4 tetrahedra as in zircon and direct linkages between Zr polyhedra. The trend to have Zr segregation within the aluminosilicate structure prefigures the structural organization that prevails in Zr-rich crystalline phases, which favors ZrO_2 precipitation [48]. As shown in Fig. 1, ZrO_2 crystals are expected for high Zr amount. Zircon is predicted at all compositions but at relatively low temperature and their presence can be bypassed by rapid quenching of the melt.

The evolution of Zr environment with ZrO_2 content could strongly affect the macroscopic glass properties and the glass durability in particular. For instance alkali resistant glass fibers used as reinforcement materials for cements contain a high proportion of ZrO_2 (17wt%) that prevents the attack of the silicate network by hydroxyl OH^- ions [7]. This is probably due to the formation of amorphous or distorted hydrated Zr oxides (HZO). The HZO layer forms a Zr-rich protective surface barrier that inhibits further attack [48]. The $^{[7]}$Zr sites present at high ZrO_2 content are also the dominant sites in amorphous HZO, as observed by Zr $L_{2,3}$ edges [36], which could favor the HZO formation.

In nuclear waste glasses, similar glass alteration occurs but the mechanism is complex and strongly dependent on the Zr concentration. The short term dissolution kinetics is slowed down significantly with increasing ZrO_2 content whereas, in the long term, the degree of corrosion is very high in near-saturated conditions which was explained by the persistence of Si-O-Zr bonds in the surface layer [36][6][49]. The Si-O-Zr linkages are less prone to hydrolysis compared to Si-O-Si linkages, which prevents reorganization and porosity closure of the alteration gel. HZO were inferred by Zr $L_{2,3}$-edges XANES spectra during alteration of nuclear waste glasses in undersaturated conditions and their apparition results from the leaching of the charge compensators [36].

The Zr-O average distance of 2.09 Å derived by EXAFS analysis is consistent with a majority of ZrO_6 octahedra and indicates a most probable association with Na as preferential charge balancing cations [6]. Indeed, calcium silicate glasses exhibit a Zr-O distance at 2.14 Å

and this lengthening of the Zr-O bond is ascribed to the higher field strength of Ca^{2+} compared to Na^{+} [12][42]. In the quaternary Na_2O-CaO-Al_2O_3-SiO_2 system, Molecular Dynamics simulations and ^{17}O 3Q-MAS NMR also suggest that Ca^{2+} cations show a preferential interaction with the non-bridging oxygen [50][51]. A negative charge excess on the $(ZrO_6)^{2-}$ octahedra requires a local charge compensation that is bring by two positive charges from alkali or alkaline-earth ions. This is similar to the charge stabilization of the $(AlO_4)^{-}$ group and, thereby, Al and Zr behaves similarly by capturing charge-balancing cations. For both elements, the charge balancing is more effective with Na rather than Ca [44]. A competition can occur for the charge balance of AlO_4 and ZrO_6 units and the addition of ZrO_2 within the glass structure increases this competition.

Whatever the ZrO_2 content, ^{27}Al NMR spectra indicate that aluminum is always four-fold coordinated to oxygen. In the case of 0ZrAl, given the composition of the glass and the affinity of aluminum for sodium, the negative charge of $^{[4]}Al$ is charge compensated by Na^{+}. This is confirmed by the small value of the quadrupolar coupling constant measured on ^{27}Al NMR spectrum (i.e. 4.6 MHz). This value increases when ZrO_2 content increases indicating that an increasing part of $^{[4]}Al$ is charge compensated by a cation with higher field strength than Na^{+}. This suggests that part of Na^{+} is enlisted to charge compensated $^{[6]}Zr$ sites and that $^{[4]}Al$ tetrahedra are progressively compensated by Ca^{2+}. When the ZrO_2 content increases (16ZrAl), not enough Ca and Na are available to charge compensate both Al and Zr sites. As a result, the coordination of Zr increases and its environment is less stabilized within the glass structure which triggers ZrO_2 crystallization.

5.2. Zr-O-Zr linkages

EXAFS analysis provide information regarding the second shell environment in the surroundings of Zr. A Zr-Zr distance near 3.3-3.4 Å is indicative of Zr-Zr clustering. The Zr-Zr average distance increases with increasing ZrO_2 content. This result is counter-intuitive because the higher the number of zirconium atoms, the lower the average distance between two atoms is expected. This evolution of the Zr-Zr distances is likely related to the Zr coordination increase with ZrO_2. Indeed for the ZrO_2-rich samples, the interatomic Zr-Zr distance is close to that in Baddeleyite at 3.460 Å in which Zr is 7-fold coordinated [41]. This increase in Zr-Zr distances could therefore implies a pre-organization towards the formation of Baddeleyite (which is not observed by X-ray diffraction) as ZrO_2-rich compositions are near the Zr saturation limit. This result is therefore consistent with the slight increase in the average

coordination number of oxygen atoms around Zr. The high coordinated Zr species are abundant for glasses with high zirconia content and the Zr local environment and the segregation of Zr polyhedra have probably important role in the nucleation of ZrO_2.

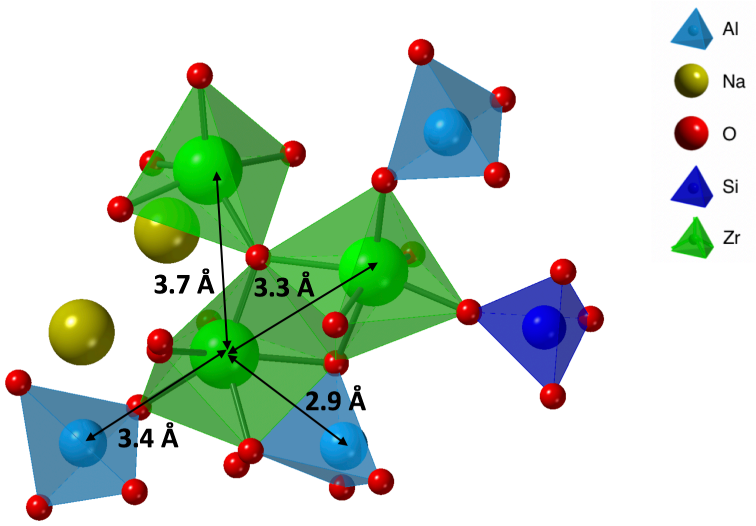

Fig. 12. Schematic representation of ZrO_6 unit linked with $(Si,Al)O_4$ and ZrO_x units and distances between Zr and the Zr or (Si,Al) neighbors.

5.3. Influence of ZrO_2 content on the aluminosilicate network

The addition of zirconium into the glass decreases the amount of Q^3 species in favor of Si-O-Zr bonds designed as $Q^3(Zr)$. The $Q^3(Zr)$ Raman band confirms the presence of Si atoms as a second neighbor near Zr, also detected by EXAFS (Table 2). The addition of zirconium would therefore lead to the transformation of silicon linked with three network forming units (SiO_4 or AlO_4) and one non-bridging oxygen (NBO) to a silicon linked with four network forming units, considering Zr as a network former. With the addition of ZrO_2, more cations are required for charge balancing Zr sites yielding fewer nonbridging oxygen species and a network repolymerization is expected. The strong bonding between the silicate network and Zr was directly evidenced by a signal corresponding to Si-O-Zr bonds in ^{17}O MQ-MAS NMR spectra in borosilicate glasses [52].

The higher network connectivity with the addition of ZrO_2 is in good agreement with the increased viscosity observed when zirconium is added [53] and Figure 2 in Supplementary Information.

The slight shift towards higher chemical shifts for ^{29}Si spectra and higher ZrO_2 content could have various origins: it can translate a polymerization of the silicate network or it can be due to the presence of zirconium as second neighbors. A narrowing of the ^{29}Si NMR peak is also observed in aluminoborosilicate glasses with addition of ZrO_2 and was ascribed to zirconium increasing the silicate network rigidity since angular distribution of SiO_4 tetrahedra are more constrained [44]. A strengthening of the network was also invoked by Molecular Dynamics (MD) simulations in borosilicate glasses with increasing ZrO_2 concentration up to 8 mol% ZrO_2 and ascribed to increasing amount of six-membered rings [5].

6. Conclusion

We have clarified the evolution of the structure and Zr environment in Na-Ca aluminosilicate glasses with high-zirconia content using X-ray absorption spectroscopy at Zr $L_{2,3}$ and K-edges, NMR and Raman spectroscopy. The detailed zirconium environment is presented as a function of the ZrO_2 concentration. Zr environment is mainly octahedral but high coordinated Zr species are increasing with the ZrO_2 content and reach 20-25% of Zr atoms in the most ZrO_2-rich glasses, prior the solubility limit and ZrO_2 crystallization. Increasing ZrO_2 concentration has a little effect on the Al environment indicating that that Al competes favorably over Zr to attract charge balancing cations. Experimental data can detect Si-O-Zr linkages, indicating strong connectivity between Zr polyhedra and the silicate framework, and Zr-O-Zr linkages, indicating important Zr segregation even at low ZrO_2 content. The presence of these linkages could have strong influence on the chemical durability or crystallization properties of these glasses.

Acknowledgments

The authors gratefully acknowledge the CAMPARIS microprobe department in Sorbonne University for their experimental help. We acknowledge SOLEIL (Proposal 20150961) and ELETTRA (Proposal 20165494) for beamtime and for assistance in using LUCIA and XAFS beamlines during the XANES measurements. Financial support from the IR-RMN-THC Fr3050 CNRS for conducting the research is gratefully acknowledged. We also like to thank Olivier Beyssac for his kind help with the Raman spectra acquisition and Laurence Galoisy for valuable discussions.

References

[1] A.J. Connelly, N.C. Hyatt, K.P. Travis, R.J. Hand, E.R. Maddrell, R.J. Short, The structural role of Zr within alkali borosilicate glasses for nuclear waste immobilisation, J. Non-Cryst. Solids. 357 (2011) 1647–1656.

[2] L.J. Manfredo, R.N. McNally, Solubility of Refractory Oxides in Soda-Lime Glass, J. Am. Ceram. Soc. 67 (1984) C-155-C–158.

[3] R. Karell, J. Kraxner, M. Chromcikova, M. Liska, Properties of selected zirconia containing silicate glasses II, Ceram. - Silikáty. 51 (2007) 125–130.

[4] J.G. Fisher, P.F. James, J.M. Parker, Soda lime zirconia silicate glasses as prospective hosts for zirconia-containing radioactive wastes, J. Non-Cryst. Solids. 351 (2005) 623–631.

[5] X. Lu, L. Deng, S. Gin, J. Du, Quantitative Structure–Property Relationship (QSPR) Analysis of ZrO2-Containing Soda-Lime Borosilicate Glasses, J. Phys. Chem. B. 123 (2019) 1412–1422.

[6] B. Bergeron, L. Galoisy, P. Jollivet, F. Angeli, T. Charpentier, G. Calas, S. Gin, First investigations of the influence of IVB elements (Ti, Zr, and Hf) on the chemical durability of soda-lime borosilicate glasses, J. Non-Cryst. Solids. 356 (2010) 2315–2322.

[7] R.G. Simhan, Chemical durability of ZrO_2 containing glasses, J. Non-Cryst. Solids. 54 (1983) 335–343.

[8] F. Farges, C.W. Ponader, G.E. Brown, Structural environments of incompatible elements in silicate glass/melt systems: I. Zirconium at trace levels, Geochim. Cosmochim. Acta. 55 (1991) 1563–1574.

[9] G. Ferlat, L. Cormier, M.H. Thibault, L. Galoisy, G. Calas, J.M. Delaye, D. Ghaleb, Evidence for symmetric cationic sites in zirconium-bearing oxide glasses, Phys. Rev. B. 73 (2006) 214207.

[10] L. Galoisy, E. Pélegrin, M.-A. Arrio, P. Ildefonse, G. Calas, D. Ghaleb, C. Fillet, F. Pacaud, Evidence for 6-Coordinated Zirconium in Inactive Nuclear Waste Glasses, J. Am. Ceram. Soc. 82 (1999) 2219–2224.

[11] C. Meneghini, A.F. Gualtieri, C. Siligardi, Differential anomalous wide-angle X-ray scattering and X-ray absorption experiments to investigate the formation of glass ceramics in the $CaO–SiO_2–ZrO_2$ system, J. Appl. Crystallogr. 32 (1999) 1090–1099.

[12] C. Meneghini, S. Mobilio, L. Lusvarghi, F. Bondioli, A.M. Ferrari, T. Manfredini, C. Siligardi, The structure of ZrO_2 phases and devitrification processes in a Ca–Zr–Si–O-based glass ceramic: a combined a-XRD and XAS study, J. Appl. Crystallogr. 37 (2004) 890–900.

[13] P. Jollivet, G. Calas, L. Galoisy, F. Angeli, B. Bergeron, S. Gin, M.P. Ruffoni, N. Trcera, An enhanced resolution of the structural environment of zirconium in borosilicate glasses, J. Non-Cryst. Solids. 381 (2013) 40–47.

[14] D.A. McKeown, I.S. Muller, A.C. Buechele, I.L. Pegg, X-ray absorption studies of the local environment of Zr in high-zirconia borosilicate glasses, J. Non-Cryst. Solids. 258 (1999) 98–109.

[15] O. Dargaud, L. Cormier, N. Menguy, L. Galoisy, G. Calas, S. Papin, G. Querel, L. Olivi, Structural role of Zr4+ as a nucleating agent in a $MgO–Al_2O_3–SiO_2$ glass-ceramics: A combined XAS and HRTEM approach, J. Non-Cryst. Solids. 356 (2010) 2928–2934.

[16] O. Dargaud, G. Calas, L. Cormier, L. Galoisy, C. Jousseaume, G. Querel, M. Newville, In Situ study of Nucleation of Zirconia in an $MgO-Al_2O_3-SiO_2$ Glass, J. Am. Ceram. Soc. 93 (2010) 342–344.

[17] T. Dumas, A. Ramos, M. Gandais, J. Petiau, Role of zirconium in nucleation and crystallization of a (SiO_2,Al_2O_3,MgO,ZnO) glass, J Mater Sc Lett. 4 (1985) 129–132.

[18] L. Cormier, B. Cochain, A. Dugué, O. Dargaud, Transition Elements and Nucleation in Glasses Using X-ray Absorption Spectroscopy, Int. J. Appl. Glass Sci. 5 (2014) 126–135.
[19] D.A. McKeown, I.S. Muller, A.C. Buechele, I.L. Pegg, C.A. Kendziora, Structural characterization of high-zirconia borosilicate glasses using Raman spectroscopy, J. Non-Cryst. Solids. 262 (2000) 126–134.
[20] L.J. Larner, K. Speakman, A.J. Majumdar, Chemical interactions between glass fibres and cement, J. Non-Cryst. Solids. 20 (1976) 43–74.
[21] M.W. Gaultois, A.P. Grosvenor, XANES and XPS investigations of the local structure and final-state effects in amorphous metal silicates: $(ZrO_2)_x(TiO_2)_y(SiO_2)_{1-x-y}$, Phys Chem Chem Phys. 14 (2012) 205–217.
[22] D.M. Pickup, G. Mountjoy, G.W. Wallidge, R.J. Newport, M.E. Smith, Structure of $(ZrO_2)_x(SiO_2)_{1-x}$ xerogels (x=0.1, 0.2, 0.3 and 0.4) from FTIR, ^{29}Si and ^{17}O MAS NMR and EXAFS, Phys. Chem. Chem. Phys. 1 (1999) 2527–2533.
[23] A. Makishima, H. Oohashi, M. Wakakuwa, K. Kotani, T. Shimohira, Alkaline durabilities and structures of amorphous aluminosilicates containing ZrO_2 prepared by the chemical polymerization of metal alkoxides, J. Non-Cryst. Solids. 42 (1980) 545–552.
[24] K. Kato, N. Araki, The corrosion of zircon and zirconia refractories by molten glasses, J Non Cryst Solids. 80 (1986) 681–687.
[25] D. Vantelon, N. Trcera, D. Roy, T. Moreno, D. Mailly, S. Guilet, E. Metchalkov, F. Delmotte, B. Lassalle, P. Lagarde, A.-M. Flank, The LUCIA beamline at SOLEIL, J. Synchrotron Radiat. 23 (2016) 635–640.
[26] C. Biagioni, E. Bonaccorsi, N. Perchiazzi, S. Merlino, Single crystal refinement of the structure of Baghdadite from Fuka (Okayama Prefecture, Japan), Period. Mineral. (2010) 01–09.
[27] D.K. Smith, W. Newkirk, The crystal structure of baddeleyite (monoclinic ZrO_2) and its relation to the polymorphism of ZrO_2, Acta Crystallogr. 18 (1965) 983–991.
[28] K. Robinson, G.V. Gibbs, P.H. Ribbe, The structure of zircon: a comparison with garnet, Amer Min. 56 (1971) 782–790.
[29] B. Ravel, M. Newville, ATHENA, ARTHEMIS, HEPHAESTUS: data analysis for X-ray absorption spectroscopy using IFEFFIT, J Synchrotron Rad. 12 (2005) 537–541.
[30] A. Di Cicco, G. Aquilanti, M. Minicucci, E. Principi, N. Novello, A. Cognigni, L. Olivi, Novel EXAFS capabilities at ELETTRA synchrotron light source, J Phys Conf. Ser. 190 (2009) 012043.
[31] S.I. Zabinsky, J.J. Rehr, A. Ankudinov, R.C. Albers, M.J. Eller, Multiple-scattering calculations of x-ray-absorption spectra, Phys. Rev. B. 52 (1995) 2995–3009.
[32] D.A. Long, Raman spectroscopy, McGraw-Hill, 1977.
[33] D. Massiot, F. Fayon, M. Capron, I. King, S. Le Calve, B. Alonso, J.O. Durand, B. Bujoli, Z.H. Gan, G. Hoatson, Modelling one- and two-dimensional solid-state NMR spectra, Mag Res Chem. 40 (2002) 70–76.
[34] H. Li, L. Li, D.M. Strachan, M. Quian, J. Cheng, L. Tang, Corrosion of electrocast AZS refractories by CAS glass–ceramics melting. J. Non Cryst. Solids 354 (2008) 1418–1423.
[35] P. Šimurka, J. Kraxner, P. Vrábel, T. Pauco, Corrosion of AZS refractories - Source of defects in tableware glass, in: 76th Conference on Glass Problems, Ceramic Engineering and Science Proceedings. Wiley, Columbus, Ohio, (2016) 89–102.
[36] E. Pelegrin, G. Calas, P. Ildefonse, P. Jollivet, L. Galoisy, Structural evolution of glass surface during alteration: Application to nuclear waste glasses, J Non-Cryst Solids. 356 (2010) 2497–2508.
[37] L. Cormier, O. Dargaud, G. Calas, C. Jousseaume, S. Papin, N. Trcera, A. Cognigni, Zr

environment and nucleation role in aluminosilicate glasses, Mater Chem Phys. 152 (2015) 41–47.
[38] H. Ikeno, M. Krause, T. Höche, C. Patzig, Y. Hu, A. Gawronski, I. Tanaka, C. Rüssel, Variation of Zr-$L_{2,3}$ XANES in tetravalent zirconium oxides, J. Phys. Condens. Matter. 25 (2013) 165505.
[39] F. Farges, Does Zr-F "complexation" occur in magmas?, Chem. Geol. 127 (1996) 253–268.
[40] P. Li, I.-W. Chen, J.E. Penner-Hahn, X-ray-absorption studies of zirconia polymorphs. I. Characteristic local structures, Phys. Rev. B. 48 (1993) 10063–10073.
[41] C.J. Howard, R.J. Hill, B.E. Reichert, Structures of the ZrO2 Polymorphs at Room Temperature by High-Resolution Neutron Powder Diffraction, Acta Cryst B. 44 (1988) 116–120.
[42] A. Quintas, D. Caurant, O. Majérus, P. Loiseau, T. Charpentier, J.-L. Dussossoy, ZrO_2 addition in soda-lime aluminoborosilicate glasses containing rare earths: Impact on rare earths environment and crystallization, J. Alloys Compd. 719 (2017) 383–391.
[43] S.W. Lee, R.A. Condrate, The infrared and Raman spectra of ZrO_2-SiO_2 glasses prepared by a sol-gel process, J. Mater. Sci. 23 (1988) 2951–2959.
[44] F. Angeli, T. Charpentier, D. de Ligny, C. Cailleteauz, Boron Speciation in Soda-Lime Borosilicate Glasses Containing Zirconium, J Am Ceram Soc. 93 (2010) 2693–2704.
[45] C. Le Losq, D.R. Neuville, P. Florian, G.S. Henderson, D. Massiot, The role of Al^{3+} on rheology and structural changes in sodium silicate and aluminosilicate glasses and melts, Geochim. Cosmochim. Acta. 126 (2014) 495–517.
[46] D.R. Neuville, L. Cormier, D. Massiot, Al coordination and speciation in calcium aluminosilicate glasses: effects of composition determined by ^{27}Al MQ-MAS NMR and Raman spectroscopy, Chem Geol. 229 (2006) 173–185.
[47] O. Dargaud, L. Cormier, N. Menguy, G. Patriarche, G. Calas, Mesoscopic scale description of nucleation processes in glasses, Appl Phys Lett. 99 (2011) 021904.
[48] V.T. Yilmaz, Chemical attack on alkali-resistant glass fibres in a hydrating cement matrix: characterization of corrosion products, J. Non-Cryst. Solids. 151 (1992) 236–244.
[49] C. Cailleteau, F. Angeli, F. Devreux, S. Gin, J. Jestin, P. Jollivet, O. Spalla, Insight into silicate-glass corrosion mechanisms, Nat. Mater. 7 (2008) 978–983.
[50] L. Cormier, D.R. Neuville, Ca and Na environments in Na_2O–CaO–Al_2O_3–SiO_2 glasses: influence of cation mixing and cation-network interactions, Chem. Geol. 213 (2004) 103–113.
[51] S.K. Lee, S. Sung, The effect of network-modifying cations on the structure and disorder in peralkaline Ca–Na aluminosilicate glasses: O-17 3QMAS NMR study, Chem. Geol. 256 (2008) 326–333.
[52] F. Angeli, T. Charpentier, M. Gaillard, P. Jollivet, Influence of zirconium on the structure of pristine and leached soda-lime borosilicate glasses: Towards a quantitative approach by O-17 MQMAS NMR, J Non-Cryst Solids. 354 (2008) 3713–3722.
[53] M. Ficheux, Diffusion multicomposante et environnement structural dans le verre Na_2O-CaO-Al_2O_3-SiO_2 contenant du zirconium, Sorbonne Université, 2018.

SUPPLEMENTARY INFORMATION

Table SI1 : Results of fit using linear combination of spectra characteristic of [6]Zr, [7]Zr and [8]Zr. For each sample, three combinations are presented: x*5ZrAl+y*mZrO$_2$+z*ZrSiO$_4$, *5ZrAl+y*mZrO$_2$ and x*5ZrAL+z*ZrSiO$_4$). x, y and z are given for the three linear combination and are fractions adding up to 1.

R-factor is the goodness quality of the fit ($R_{factor} = (\sum(data - fit)^2)/\sum data^2$). E_0 is the edge energy for each spectra to fix up any inconsistencies in energy alignment (Ravel and Newville, 2005).

Sample	x	y	z	R-factor (10^{-3})	E_0 (eV)
7.5Zr	0.898	0.057	0.045	0.1525	-0.011 -0.089 -0.355
	0.907	0.083		0.2047	-0.012 -0.404
	0.886		0.114	0.2924	-0.011 -0.106
10Zr	0.826	0.083	0.092	0.1690	-0.016 -0.133 -0.239
	0.844	0.156		0.4084	-0.016 -0.102
	0.809		0.191	0.4864	-0.016 -0.102
12Zr	0.765	0.129	0.106	0.3258	-0.015 -0.089 -0.726
	0.785	0.215		0.7306	-0.019 -0.69
	0.739		0.261	1.2963	-0.011 -0.353
15Zr	0.800	0.038	0.163	2.0803	-0.027 2.057 -0.686
	0.788		0.212	2.2482	-0.023 -0.49
	0.828	0.172		3.3164	-0.032 -0.825
16Zr	0.557	0.226	0.217	0.7715	-0.019 -0.223 -0.828
	0.599	0.401		3.2931	-0.030 -0.958
	0.511		0.489	5.3089	-0.005 -0.470

Figure SI-1 : Proportion of [6]Zr species as reported in Table SI-1 as a function of ZrO_2 content. The 5ZrAl sample has been arbitrarily fixed at 100% [6]Zr.

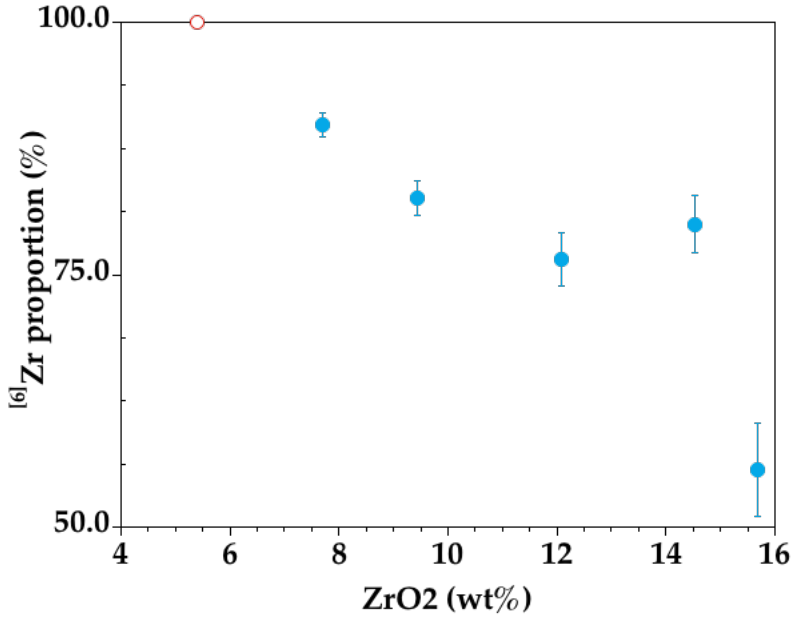

Figure SI-2 : Viscosities for the glass investigated in this study.